

Simulation of 0–7.5 Hz physics-based nonlinear ground motions for maximum credible earthquake scenarios at the Long Valley Dam, CA

Earthquake Spectra

1–28

© The Author(s) 2024

Article reuse guidelines:

sagepub.com/journals-permissions

DOI: 10.1177/87552930231226135

journals.sagepub.com/home/eqs

Te-Yang Yeh,  EERI, and Kim Bak Olsen

Abstract

We have conducted three-dimensional (3D) 0–7.5 Hz physics-based wave propagation simulations to model the seismic response of the Long Valley Dam (LVD), which has formed Lake Crowley in Central California, to estimate peak ground motions and settlement of the dam expected during maximum credible earthquake (MCE) scenarios on the nearby Hilton Creek Fault (HCF). We calibrated the velocity structure, anelastic attenuation model, and the overall elastic properties of the dam via linear simulations of a M_w 3.7 event as well as the M_w 6.2 Chalfant Valley earthquake of 1986, constrained by observed ground motions on and nearby the LVD. The Statewide California Earthquake Center (SCEC) Community Velocity Model CVM-S4.26.M01 superimposed with a geotechnical layer using V_{S30} information tapered from the surface to a 700-m depth was used in the simulations. We found optimal fit of simulated and observed ground motions at the LVD using frequency-independent attenuation of $Q_s = 0.075V_s$ (V_s in m/s). Using the calibrated model, we simulated 3D nonlinear ground motions at the LVD for M_w 6.6 rupture scenarios on the HCF using an Iwan-type, multi-yield-surface technique. We use a two-step method where the computationally expensive nonlinear calculations were carried out in a small domain with the plane wave excitation along the bottom boundary obtained from a full-domain 3D linear finite-fault simulation. Our nonlinear MCE simulation results show that peak ground velocities (PGVs) and peak ground accelerations (PGAs) as high as 72 cm/s and 0.55 g, respectively, can be expected at the crest of the LVD. Compared with linear ground motion simulation results, our results show that Iwan nonlinear damping reduces PGAs on the dam crest by up to a factor of 8 and increasingly depletes the high-frequency content of the waves toward the dam crest. We find horizontal

Department of Earth & Environmental Sciences, San Diego State University, San Diego, CA, USA

Corresponding author:

Te-Yang Yeh, Department of Earth & Environmental Sciences, San Diego State University, 5500 Campanile Drive, San Diego, CA 92182, USA.

Email: tyeh2@sdsu.edu

relative displacements of the material inside the dam of up to 27 cm and up to 55 cm of vertical subsidence, equivalent to 1% of the dam height.

Keywords

Long Valley Dam, maximum credible earthquake, Hilton Creek Fault, wave propagation, nonlinear response

Date received: 19 June 2023; accepted: 12 December 2023

Introduction

Failure of dams during seismic shaking can have devastating societal consequences. While well-designed Earth dams have generally performed well during earthquake ground shaking (FEMA, 2005), catastrophic failures have occurred due to the ground shaking level, structure design, and material properties (FEMA, 2005; Seed et al., 1978). Here, we have carried out three-dimensional (3D) numerical simulations to predict the seismic response of the Long Valley Dam (LVD) for a maximum credible earthquake (MCE). The LVD is a 55-m high embankment dam located 35 km northwest of Bishop, CA, just east of the Sierra Nevada range (see Figure 1). The completion of the dam in 1941 created Lake

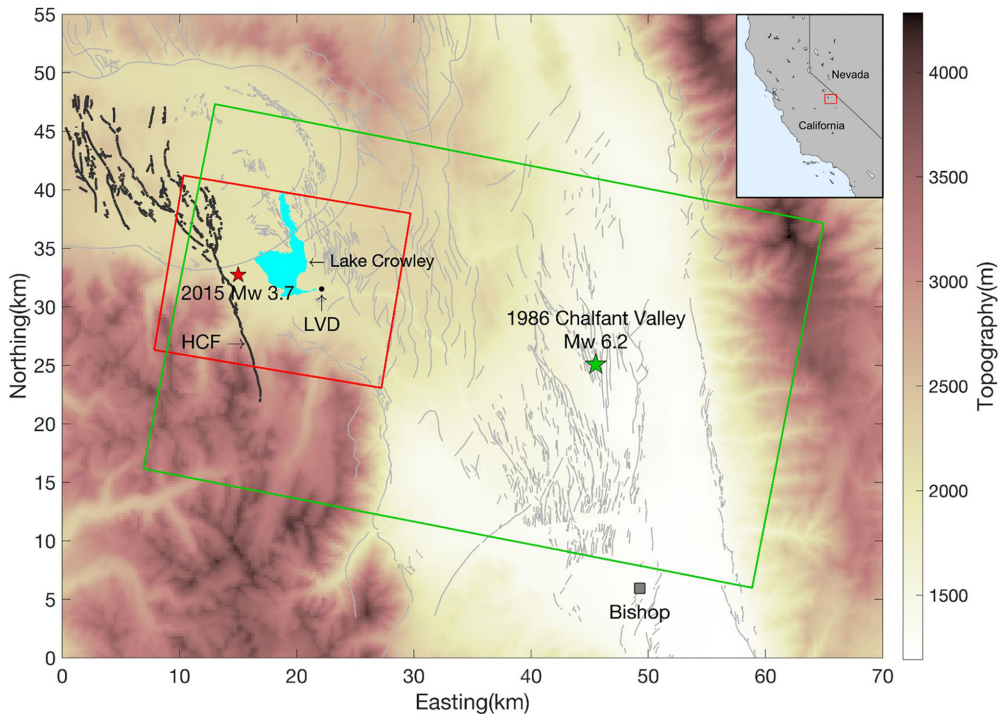


Figure 1. Map showing locations of the Long Valley Dam (black dot), Lake Crowley (blue-shaded area), and model domains for (red rectangle) the simulations of the M_w 3.7 earthquake of 2015 and (green rectangle) the 1986 Chalfant Valley earthquake. Quaternary faults (Haller et al., 2004) are depicted by gray lines where fault segments of the Hilton Creek fault (HCF) system are highlighted with thick black lines. Red box in the upper right inset shows the general location of the area on this map.

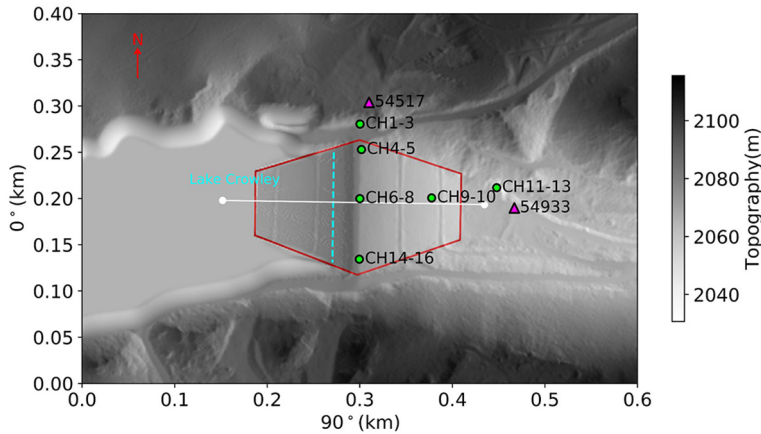


Figure 2. Map view of the Long Valley Dam (see Figure 1 for the general location). The blue dashed line depicts the lake water surface on the upstream face. Green-filled circles are sensor locations of the structure array (station code 54214) installed on the LVD (within red line). Magenta triangles depict nearby ground stations also included in our analysis. The white line shows the location of the cross section used to display peak ground motions, permanent deformation, and shear modulus reduction inside the dam. Grayscale shading depicts topography.

Crowley, which has served as a storage unit for the Los Angeles aqueduct as well as a flood control unit. The major part of the dam consists of extensive rolled earthfill core (Lai and Seed, 1985). The dam has an array of accelerometers located on the dam crest, downstream wall, and abutments and downstream riverbed (see section “Data and resources” for data access), which provide useful seismic data for studies of seismic response of the dam (Figure 2).

To study the response of an embankment dam under seismic loading, site-specific characteristics must be considered. The seismic response of the LVD has been extensively studied in which the soil behavior was modeled by different approaches. For example, Lai and Seed (1985) accounted for the nonlinear response of the dam materials by using equivalent linear soil properties. Later studies used more rigorous numerical methods (e.g. finite elements and finite differences) to simulate the nonlinear hysteretic behavior of the dam materials under cyclic loading with multi-surface plasticity theory (Griffiths and Prevost, 1988; Yiagos and Prevost, 1991; Zeghal and Abdel-Ghaffar, 1992). A potential limitation of the earlier studies arises from the treatment of the excitation of the dam. Typically, stability analyses for dams use accelerograms of historical events, for example, recorded near the downstream base, as input motion. This approach is restricted by the availability of seismic records for a desired focal mechanism and event size appropriate for the targeted scenario, and usually requires potentially unphysical scaling of the input motion for different size events (Cascone et al., 2021; Ebrahimian, 2011; Elia and Rouainia, 2013; Pelecanos et al., 2012; Zou et al., 2013) that can bias the resulting ground motion (Wen et al., 2020). Another simplification in earlier studies arises from neglecting coupling of the dam with the underlying and surrounding geological layers. Conventionally, the dam is placed on top of bedrock, where an input ground motion is applied along the bottom of the dam, neglecting any effects from underlying and surrounding geological layers (e.g. Ebrahimian, 2011; Griffiths and Prevost, 1988). These simplifications are no longer required when

utilizing 3D physics-based numerical simulations with appropriate constitutive models along with well-designed source rupture models.

The Hilton Creek Fault (HCF) is a significant range-bounding normal fault on the eastern side of the Sierra Nevada. Because it passes just 8 km west of the LVD, it has been identified as a source for the MCE that could potentially damage the LVD (Lai and Seed, 1985). Scenario earthquakes on the HCF were also considered in a recent study on earthquake hazards for the Long Valley Caldera-Mono Lake Area by Chen et al. (2014). However, the methods used in that study were based primarily on ground motion models (GMMs) which provide only peak ground motion amplitudes and spectral accelerations. In addition, GMM-based approaches provide only rudimentary control on the effects of source parameters, with no support of physical quantities needed for stability analysis of the dam (e.g. stress, strain), or the complete time history of particle motions (FEMA, 2005). In this study, we performed coupled 3D physics-based simulations considering both linear and nonlinear response of the material within the LVD and its surroundings. We avoid the conventional selection and scaling of a seismic record as source function using a two-step simulation method, consisting of (1) a linear 3D simulation of the HCF MCE finite-fault scenario and (2) a multi-yield-surface nonlinear 3D simulation in a much smaller model including the LVD and all the 3D structures around it, using the seismic motion below the LVD from (1) as excitation (see section “HCF scenario ground motion results”).

The first part of this study consists of the validation of the velocity model and calibration of the parameters of the attenuation model, geotechnical layer (GTL), and 3D structure of the dam, with two validation events. The first validation event is a M_w 3.7 earthquake of 2015 located 7 km to the west of the LVD, where we used a point source representation. The second validation event is the M_w 6.2 Chalfant Valley earthquake of 1986, where we used the Graves and Pitarka (2016) kinematic rupture generator to produce realizations of finite-fault source models. The second part of this work is to design various rupture scenarios along the HCF, attempting to find the scenario that represents an MCE for the LVD. The final part provides predictions of peak ground motions as well as the relative displacements inside the LVD that can be expected during the proposed M_w 6.6 MCE scenario.

Numerical method

We carried out 3D wave propagation simulations in an earth model including the LVD up to 7.5 Hz with the fourth-order accurate finite-difference (FD) code AWP-ODC (with suffix derived from authors’ last names, Olsen, Day, and Cui), which is highly scalable on graphics processing unit (GPU) platforms and has support for surface topography and frequency-dependent attenuation (Cui et al., 2013; Olsen, 1994; O’Reilly et al., 2022; Withers et al., 2015). To reduce computational cost, we used three mesh blocks separated vertically with a factor-of-three increase in grid spacing with depth (3.5, 10.5, and 31.5 m) for our simulations via a discontinuous mesh approach (Nie et al., 2017). This approach requires an overlap zone of width $7 dx_f$, where dx_f is the smaller grid spacing of the two mesh blocks, as indicated by the depth range of each mesh block listed for models with different simulation domains (see Tables 1, 3 and 6). We used a minimum shear wave velocity of 175 m/s in the top block, ensuring at least 6.7 points per minimum wavelength (O’Reilly et al., 2022).

For the nonlinear HCF simulations, we use a multi-surface, 3D nonlinear model Roten et al. (2023) implemented in AWP-ODC. The method adopts the overlay concept (Iwan, 1967; Mróz, 1967) by combining a large number of spring sliders (Kaklamanos et al., 2015). Each spring slider is an individual component that represents a (von Mises) yield surface with a pre-calculated yield level, in which the unit follows elastic, perfectly-plastic behavior. The spring sliders are arranged in a parallel-series configuration to reproduce the hysteretic behavior described by the Masing rule (Masing, 1926) that is frequently used to describe nonlinear soil behavior. The accuracy of the method converges for 7-10 yield surfaces or more (Kaklamanos et al., 2015; Roten et al., 2023). The resulting hyperbolic model (Hardin and Drnevich, 1972) captures the nonlinear response of the soil, which describes the reduction of the shear modulus of the uniaxial simple shear as:

$$\frac{G}{G_0} = \frac{1}{1 + \frac{\gamma_{xy}}{\gamma_r}}, \quad (1)$$

where G_0 is the maximum shear modulus, γ_{xy} is shear strain, and γ_r is the reference strain. The reference strain is a key parameter that characterizes the nonlinear behavior of the material in our nonlinear method. The reference strain is defined as:

$$\gamma_r = \frac{\tau_0}{G_0}, \quad (2)$$

where τ_0 is the yield stress, which is the maximum shear stress that the material can support under the initial stress state (Roten et al., 2012). This expression is useful since the yield stress can be estimated in various ways. To compute τ_0 , the cohesion (C) and the friction angle (ϕ) are needed, given as:

$$\tau_0 = C \cos(\phi) - (\sigma_m - P) \sin(\phi), \quad (3)$$

where P is the fluid pressure, and σ_m is the effective mean stress. For simplicity, we used the lithostatic stress as a proxy for σ_m in the calculation of yield stress.

Support for surface topography is essential to model the seismic response of the LVD. For the validation work of the 2015 M_w 3.7 event, we used the curvilinear grid approach by O'Reilly et al. (2022). However, this version of AWP-ODC does not yet support nonlinear soil response calculations. For this reason, we performed the validations for the 1986 M_w 6.2 Chalfant Valley event and simulations of the M_w 6.6 HCF scenarios using a Cartesian grid FD code with a vacuum formulation as the free surface boundary (Graves, 1996; Randall, 1989; Zahradník et al., 1993). These previous studies clearly show that the accuracy of the vacuum formulation is reduced, as compared with explicit free surface formulations. However, we verified the seismic response of the LVD using the vacuum formulation, as compared with those from the curvilinear solution, ensuring that the topographic response of the LVD predicted by the vacuum formulation is sufficiently accurate for the current application (see ‘‘Accuracy of the vacuum formulation’’ section in the Supplemental Material, Figures S1 to S3).

Velocity model

Our reference model is extracted from the Statewide California Earthquake Center (SCEC) Community Velocity Model (CVM) version S4.26.M01 (CVM-S from here on)

(Small et al., 2017). It has been shown (Ely et al., 2010; Hu et al., 2022b) that the CVM-S generally causes underprediction of peak amplitudes and coda duration outside the major basins in Southern California due to unrealistically high near-surface velocities. To alleviate this underprediction, Ely et al. (2010) proposed a simple generic overlay-based tapering, considering the time-averaged shear wave velocity (V_S) in the top 30 m (i.e. V_{S30}) and merging with the tomography at a depth of 350 m, which can be applied to any of the velocity models accessible through the SCEC Unified Community Velocity Model (UCVM). Hu et al. (2022b) found that applying the taper to deeper depths (700–1000 m) significantly improved the fit between physics-based synthetics and strong-motion data for the M_w 5.1 La Habra earthquake of 2014 in the greater Los Angeles area. Following this approach, we estimated the optimal tapering depth for the near-surface material surrounding the LVD in the Sierra Nevada Mountains.

For the surface topography, we used the 1 m-resolution digital elevation model (DEM) from the US Geological Survey (2020). This DEM does not provide elevations of areas under water, including part of the upstream face of the LVD and the entire Lake Crowley. To include the lake water directly into our simulations, we made the following adjustments to the DEM. First, we removed the lake water from the DEM by manually lowering the elevations of the grids located inside the lake from 2066 m to 2036 m, assuming a flat lake bed and an average water depth of 30 m. Second, we mirrored the surface elevations of the downstream face to the upstream side with respect to the center line of the crest of the dam (axis of the dam), assuming symmetry of the LVD with respect to the axis of the dam. We then applied Gaussian filters of 7 m resolution to smooth the topography around the edges of the area where we removed the lake water, to minimize artifacts introduced by these adjustments. In our calculations, the lake water is modeled as a purely elastic material with P-wave speed (V_P) of 1050 m/s, $V_S = 0$ m/s, and density (ρ) of 1492 kg/m³, and the bathymetry of areas under lake water, including the lower portion of the upstream face, are described in a staircase fashion, following the Okamoto and Takenaka (2005) approach (see Supplemental Material).

Earlier studies have modeled the structure of the LVD with an extensive rolled earthfill clay core, which constitutes the major portion of the dam structure, with a thin layer of more permeable rock-fill shell on top (Griffiths and Prevost, 1988; Lai and Seed, 1985; Yiagos and Prevost, 1991). We explored different V_S for the homogeneous dam core as well as more complicated descriptions (see the section “Elastic properties of the LVD”). Based on our analysis, we assumed a homogeneous dam for our simulations ($V_S = 450$ m/s).

Anelastic attenuation implementation

In our simulations, we adopted a frequency-dependent attenuation model where Q_s values are given as:

$$\begin{aligned} Q_s(f) &= Q_{s,0}, & f < f_0, \\ Q_s(f) &= Q_{s,0} \left(\frac{f}{f_0} \right)^\gamma, & f \geq f_0, \end{aligned} \quad (4)$$

where the power-law exponent γ , ranging from 0 to 0.9, controls the rate of increase of Q_s above the transition frequency, f_0 , set at 1 Hz (Withers et al., 2015), and $Q_{s,0}$ is a constant Q_s value. We assumed $Q_{s,0}$ to be proportional to the local S-wave speed, $Q_{s,0} = kV_S$, where k is a parameter specific to the study area. For simplicity, the relationship of $Q_p = 2Q_s$ was

assumed throughout this study, following the findings of Olsen et al. (2003). The parameters k and γ were estimated using both validation events (see the sections “Validation I: 2015 M3.7 event” and “Validation II: The M_w 6.2 Chalfant Valley earthquake of 1986).

Data and goodness-of-fit calculation

For the model validations, we focused on ground accelerations from strong-motion sensors, including a structure array 54214 on the LVD and the surrounding ground stations 54517 and 54933 (see Figure 2 for locations), all operated under the California Strong Motion Instrumentation Program (CSMIP) with network code CE (California Geological Survey, 1972). The strong-motion data obtained from the Center for Engineering Strong Motion Data (CESMD) website (see section “Data and resources”) has been pre-processed to remove the instrument response and baseline drift. We used a goodness-of-fit (GOF) measure to quantify the differences between simulated and recorded ground motions in our search for optimal parameters of the near-surface material, and $Q(f)$ parameters. The GOF estimate is defined as the natural logarithm of the observed-to-simulated acceleration Fourier amplitude spectral ratio, given as:

$$GOF_{FAS}(f) = \ln\left(\frac{FAS_{obs}(f)}{FAS_{model}(f)}\right), \quad (5)$$

where $FAS_{obs}(f)$ and $FAS_{model}(f)$ are Fourier amplitude spectra of observed and simulated acceleration waveforms, respectively. A Savitzky–Golay filter (Savitzky and Golay, 1964) with a 0.5 Hz window length was applied to both observed and simulated spectra to suppress large fluctuations before computing the GOF. In order to minimize the effects of the baseline corrections and pre-filtering done by CESMD for the corrected strong-motion data, we compared data and simulation results from 0.4 Hz with the maximum resolved frequency in the simulations, 7.5 Hz. In this frequency band, we calculated the GOF_{FAS} (Equation 5) for all available channels for each validation event and derived the mean values and the corresponding standard deviations to quantitatively summarize the model performance at different frequencies. Note that for the definition of GOF_{FAS} , a positive value indicates underprediction and vice versa. In addition, we defined an overall error value as a summary of the mean GOF_{FAS} over the aforementioned frequency range:

$$Error = \frac{\sum_{i=1}^{Nf} |\mu_i|}{Nf}, \quad (6)$$

where μ_i is the mean GOF_{FAS} at the i th frequency point, where the arithmetic averaging is computed over Nf frequency points.

Validation I: 2015 M3.7 event

Our first validation event is a M_w 3.7 earthquake from 2015. Its small magnitude permits the approximation of the source rupture process with a point source, while the small ground motions observed at LVD (~ 0.05 g on the crest) are not expected to cause non-linear effects. For this reason, it is ideal to use this event to constrain the elastic properties of the LVD, and the proximity of the event to the HCF also makes it a reasonable choice for validation. This event has a normal faulting focal mechanism and is located 7 km to the west of the LVD (see Figure 1). We used a rotated domain to minimize computational

Table 1. Simulation parameters for the 2015 M_w 3.7 event validation

Domain	
Length	19.65 km
Width	15.12 km
Depth	14.97 km
Southwest corner	−118.8674°, 37.5385°
Northwest corner	−118.8424°, 37.6733°
Southeast corner	−118.6474°, 37.5126°
Northeast corner	−118.6221°, 37.6473°
Rotation angle	9.51° clockwise from north
Geodetic datum	WGS84
UTM zone	11
Spatial resolution	
Maximum frequency	7.5 Hz
Minimum V_S	175 m/s
Points per minimum wavelength	6.7
Grid spacing	3.5 m: Free surface to 5.03 km below sea level 10.5 m: 5.00–6.00 km below sea level 31.5 m: 5.93–14.97 km below sea level
Temporal resolution	
Time step	0.0002 s
Simulation time	20 s

UTM: Universal Transverse Mercator.

Table 2. Source parameters for the 2015 M_w 3.7 event validation

Hypocenter location (Lon., Lat., Depth)	−118.7878°, 37.5975°, 4.8 km
Origin time	2015-08-22 13:34:48 UTC (USGS)
Seismic moment	4.678×10^{14} N-m (USGS)
Focal mechanism (strike/dip/rake)	Plane 1: 158°/75°/−103° Plane 2: 20°/20°/−50°

USGS earthquake report (US Geological Survey, Earthquake Hazards Program, 2017), event ID NC72510456. Event page can be assessed via <https://earthquake.usgs.gov/earthquakes/eventpage/NC72510456/executive>. USGS: US Geological Survey; UTC: Universal Time Coordinated.

resources. See Table 1 for the configuration of the numerical simulations for the validation, and the source parameters can be found in Table 2.

Source description

To describe the source function of the M_w 3.7 event, we assumed a Brune-type moment-rate spectrum (Brune, 1970) with an f^{-2} decay at frequencies above the corner frequency (f_c), given as:

$$M(f) = \frac{M_0}{1 + (f/f_c)^2}, \quad (7)$$

where M_0 is the seismic moment. This moment-rate spectrum has a time-domain expression derived with the constraint of minimum phase:

$$M(t) = \frac{t}{T_c^2} e^{-t/T_c}, \quad (8)$$

where T_c is the characteristic time controlling the width of the pulse, which is linked to the corner frequency as $T_c = \frac{1}{2\pi f_c}$. We determined the corner frequency using:

$$f_c = k_b \beta \left(\frac{16 \Delta\sigma}{7 M_0} \right)^{\frac{1}{3}}, \quad (9)$$

where k_b is a constant, β is the V_s at the source (3,410 m/s), and $\Delta\sigma$ is the stress drop (Brune, 1970; Eshelby, 1957). Using $k_b = 0.32$ assuming a circular rupture with a rupture speed of $V_r = 0.9V_s$ (Madariaga, 1976) and a stress drop of 3 MPa (Kanamori and Anderson, 1975; Prejean and Ellsworth, 2001), we get $f_c = 2.7$ Hz which is equivalent to $T_c = 0.0593$ s (see also Supplemental Material Figure S4).

Near-surface GTL and $Q(f)$

We followed the approach of Hu et al. (2022a, 2022b) to calibrate the near-surface velocity structure within our model domain. This calibration entails replacing the velocity model extracted from the SCEC CVM-S, from the free surface to a given tapering depth (z_T) with V_P , V_S , and ρ computed using the formulations of Ely et al. (2010) along with local V_{S30} information. This approach provides a smooth transition between the near-surface velocity structures and the original model. We used the measured V_{S30} values wherever available (Yong et al., 2016), and the model values compiled by Thompson (2018) elsewhere. It should be noted that the GTL was also implemented beneath the LVD, allowing for nonlinear damping below the dam where the taper starts at the base of the dam, in agreement with the construction of the dam. However, the presence of the GTL below the dam represents a departure from classical studies of dams, where the base of the dam typically rests on top of bedrock (e.g. Griffiths and Prevost, 1988), isolating the nonlinear response to the interior of the dam.

We used a trial-and-error approach to search for the tapering depth (z_T) as well as k and γ for the anelastic attenuation that provides the best fit to the strong-motion records for the M_w 3.7 event at the LVD. To examine different z_T values for the GTL, we focused on sites off the dam to exclude the effects of the LVD. Since our synthetics reveal similar fit to data in the time and frequency domains for the tested z_T values (350, 700, and 1000 m, see Supplemental Material Figure S6; also note the strong underprediction when the GTL is omitted), we proceed with $z_T = 700$ m for the following simulations, which has been shown to generate optimal fit to data in southern California (Hu et al., 2022b; Yeh and Olsen, 2023). With this tapering depth, we found a few combinations of k and γ for anelastic attenuation that generates equally good fit to data ($k = 0.05$ and $\gamma = [0.2, 0.4]$, $k = 0.075$ and $\gamma = [0, 0.2]$, and $k = 0.1$ and $\gamma = 0$ in Supplemental Material Figure S9). See section ‘‘GTL and $Q(f)$ parameters’’ in the Supplemental Material for more details on constraining the GTL and $Q(f)$ parameters.

Elastic properties of the LVD

To select the most appropriate values for our analysis, we tested different elastic properties under low-strain conditions for the dam using the M_w 3.7 event, including the homogeneous core and the layered-type structure calculated from the elastic parameters used in

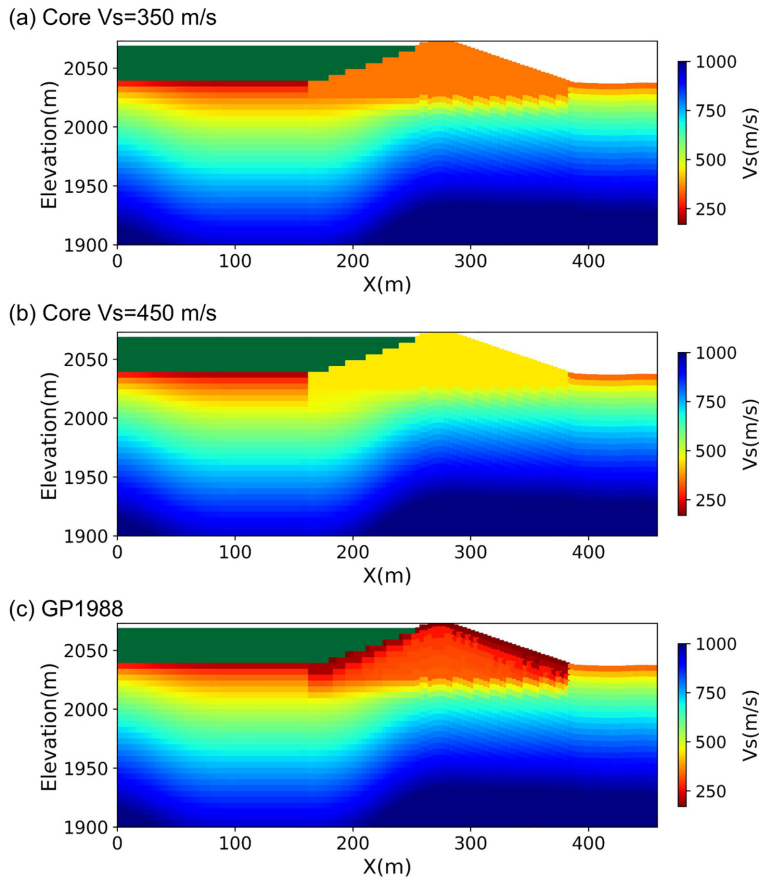


Figure 3. V_S transects across the LVD extracted from the three different dam models tested in this study. The dam core in models (a) and (b) is homogeneous, whereas (c) has a layered structure computed from the elastic parameters used in Griffiths and Prevost (1988). See Figure 2 for the location of cross section.

the numerical study by Griffiths and Prevost (1988) (see Figure 3). We note that the water–solid interface in our simulations is described in a staircase fashion, resulting in a step-like surface on the upstream side, in contrast to the smooth surface defined by the curvilinear mesh on the downstream surface. Our tests show that $V_S=450$ m/s provides the least-biased estimates of the observed ground motions in both time and frequency domains of up to 7.5 Hz among the models tested (Figure 4). See also Supplemental Material Figure S10 for a comparison of waveforms and spectra at the crest center, showing that the presence of a thin shell with low V_S values used in the Griffiths and Prevost’s (1988) modeling overpredicts the observed acceleration amplitudes by a factor of up to 2.5 on the horizontal components. In the models with a homogeneous core, we fixed the density of the core at $\rho=2110$ kg/m³ (Yiagos and Prevost, 1991), with a Poisson’s ratio at 0.4. Due to its homogeneous nature, this model makes no distinction between the core and the shell of the dam. Despite its simplicity, we note that this model is fairly close to the actual structure of LVD, as an extensive rolled earthfill clay core constitutes the major portion of the dam structure with a thin layer of more permeable rock-fill shell on top (Griffiths and Prevost, 1988; Lai and Seed, 1985; Yiagos and Prevost, 1991).

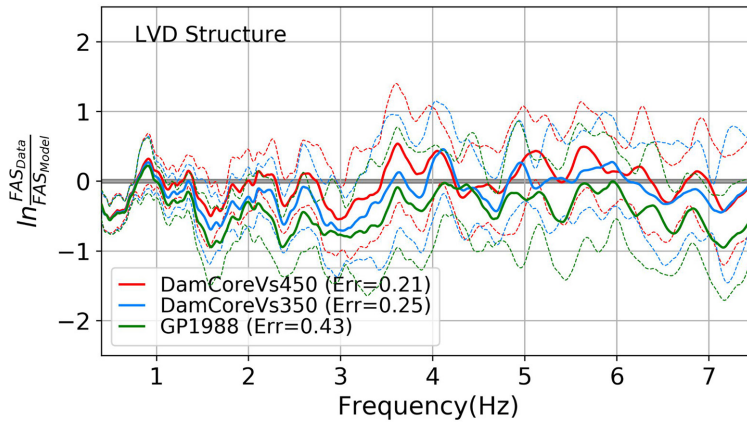


Figure 4. Comparison of spectral bias with FAS_{GOF} values computed using only sensors on the dam (channels 4–9 and 14–16) for the M_w 3.7 earthquake in 2015 (see Figure 2 for sensor locations). Using $k=0.075$, and $\gamma=0$ for the attenuation model and GTL with $z_T=700$, synthetics were computed for the three dam core models shown in Figure 3, including two homogeneous core models of $V_S = 450$ m/s (red) and $V_S = 350$ m/s (blue), and the model from Griffiths and Prevost (1988) (green).

Validation results

Figure 5 shows a comparison of synthetics from the simulation with the optimal elastic parameters of the dam ($V_P=1100$ m/s, $V_S=450$ m/s, and $\rho=2110$ kg/m³), GTL taper (700 m), and anelastic model ($Q_s=0.075V_S$, $\gamma=0$, see Supplemental Material Figure S7) to data for the M_w 3.7 event in 2015. However, we note that the anelastic attenuation has relatively small effects on the simulated ground motion due to the short source–receiver distances (see Figure S9 in Supplemental Material). Further discussion of the attenuation parameters follows in the discussion of the Chalfant Valley validation event in the following sections.

Validation II: the M_w 6.2 Chalfant Valley earthquake of 1986

Our second validation event is the M_w 6.2 Chalfant Valley earthquake of 1986. This earthquake is located 25 km to the east of the LVD, which requires a larger computational domain to accommodate the entire fault and LVD (green box in Figure 1); see Table 3 for more details about the simulation domain. The moment magnitude of this event clearly warrants a finite-fault description of its rupture. We used the Graves and Pitarka (2016) kinematic rupture generator, a widely used software tool implemented on the SCEC Broadband Platform (Maechling et al., 2014), to generate finite-fault descriptions for the Chalfant Valley event, described in the following section.

Finite-fault source model

The hypocenter locations for the Chalfant Valley earthquake reported by previous studies are fairly similar (varying horizontally ≤ 1 km), while the interpretations of the focal mechanism and the fault dimensions show larger variations (Cockerham and Corbett, 1987; Pacheco and Nábělek, 1988; Savage and Gross, 1995; Smith and Priestley, 2000). We use the published focal mechanisms for the event to assume an averaged fault

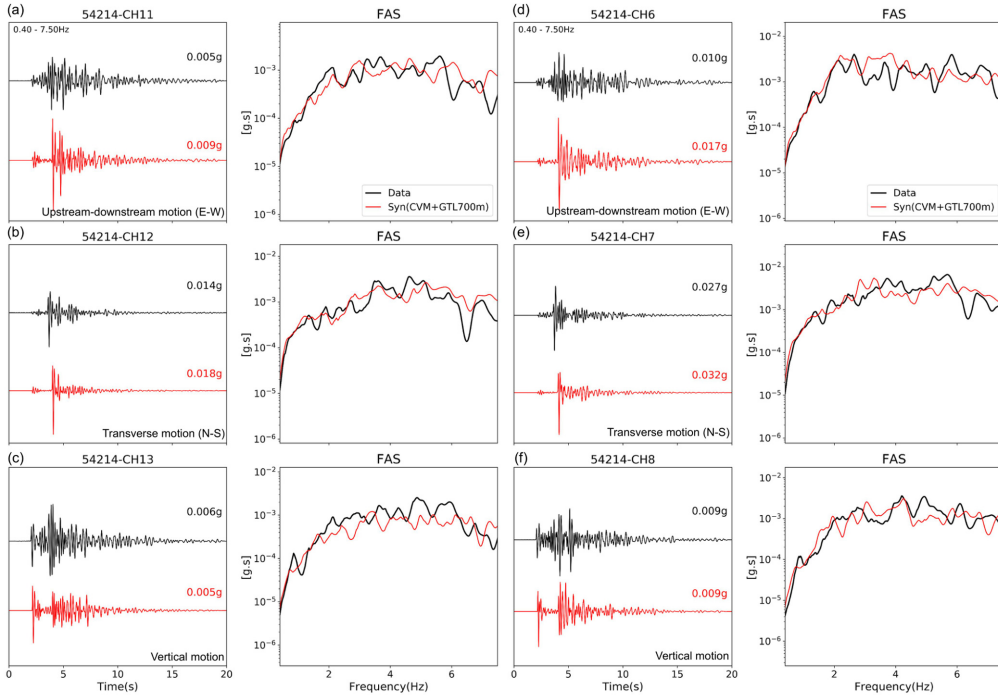


Figure 5. Comparison of data (black traces) and synthetics (red and blue traces) in the time and FAS domains at sensors located near the downstream base (a) to (c) and at the crest center (d) to (f) for the M_w 3.7 earthquake in 2015. See Figure 2 for sensor locations. The red synthetic traces were computed for CVM-S with a GTL tapered to 700 m below the free surface. Synthetics were computed with $k = 0.075$ and $\gamma = 0$ for the anelastic attenuation and a homogeneous core with $V_S = 450$ m/s for the LVD.

orientation with a pure strike-slip focal mechanism for our simulations. Following the hypocenter location and the interpreted fault length from Smith and Priestley (2000) (13.9 km), we estimated a fault width of 11.6 km using the empirical source scaling relations by Leonard (2010) for a M_w 6.2 event. Using the Graves and Pitarka (2016) kinematic rupture generator, we generated three realizations of slip distributions for the defined fault plane, focal mechanism, and hypocenter. The source parameters for this event are listed in Table 4. The slip distributions and moment-rate functions of the generated source models can be found in the Supplemental Material (Figure S11).

Validation results

We used a GTL tapered to a depth of 700 m below the free surface and a homogeneous dam core with $V_S = 450$ m/s as in the validation of the M_w 3.7 event to generate synthetic seismograms for the Chalfant Valley event. From the mean GOF_{FAS} computed with 13 available channels from structure array 54214, we found that the three finite-fault source realizations for the Chalfant Valley event result in GOF_{FAS} values between 0.22 and 0.30 averaged across the examined frequency range, suggesting that the predicted spectral response of ground motions are relatively insensitive to the choice of the random seed number defining the slip and rupture time distributions on the fault (see Figure S12 in the Supplemental Material). The largest variations in the FAS_{GOF} are found at frequencies less than 1 Hz, caused by the fact that the source descriptions used in the simulations are not

Table 3. Simulation parameters for the 1986 Chalfant Valley M_w 6.2 event validation

Domain	
Length	52.92 km
Width	31.75 km
Depth	30.75 km
Southwest corner	−118.8755°, 37.4469°
Northwest corner	−118.8134°, 37.7287°
Southeast corner	−118.2870°, 37.3631°
Northeast corner	−118.2227°, 37.6446°
Rotation angle	11.08° clockwise from north
Geodetic datum	WGS84
UTM zone	11
Spatial resolution	
Maximum frequency	7.5 Hz
Minimum V_s	175 m/s
Points per minimum wavelength	6.7
Grid spacing	3.5 m: 4.38–0.35 km above sea level 10.5 m: 0.38 km above sea level to 5.66 km below sea level 31.5 m: 5.59–30.75 km below sea level
Temporal resolution	
Time step	0.00027 s
Simulation time	30 s

UTM: Universal Transverse Mercator.

Table 4. Source parameters for the M_w 6.2 Chalfant Valley earthquake of 1986

Hypocenter location ^a (Lon., Lat., Depth)	−118.4408°, 37.5333°, 10.8 km
Origin time ^b	1986-07-21 14:42:26 (UTC)
Seismic moment ^c	2.65×10^{18} N-m
Focal mechanism (strike/dip/rake)	150°/55°/−180°
Fault dimensions ^d	Length = 13.9 km Width = 11.6 km

^aSmith and Priestley (2000).

^bUS Geological Survey earthquake report (US Geological Survey, Earthquake Hazards Program, 2017), event ID NC10085763. Event page can be assessed via <https://earthquake.usgs.gov/earthquakes/eventpage/NC10085763/executive>.

^cGlobal CMT (GCMT) project (Dziewonski et al., 1981; Ekström et al., 2012).

^dLeonard (2010); Smith and Priestley (2000).

CMT: Centroid Moment Tensor; UTC: Universal Time Coordinated.

constrained by data for the Chalfant Valley event. Nevertheless, Figure 6 (with additional comparisons in the Supplemental Material, Figure S13) shows that all three source models produced similar peak ground acceleration (PGA) values that on average fall within 35% of that from the data recorded at different locations on the LVD. Note that the Chalfant Valley earthquake validation was carried out using purely linear rheology, as the PGAs at the dam (about 0.1 g) were deemed insufficient to trigger significant nonlinear soil behavior. We find that one of the preferred attenuation models for the M_w 3.7 validation event, namely, $k = 0.075$ and $\gamma = 0$, achieves a similarly small FAS_{GOF} error range for the Chalfant Valley event (0.2–0.3, see Supplemental Material Figure S12, as well as the GTL and $Q(f)$ parameters section in the Supplemental Material for details). Therefore, these parameters will be used for the HCF scenario simulations presented in the following sections.

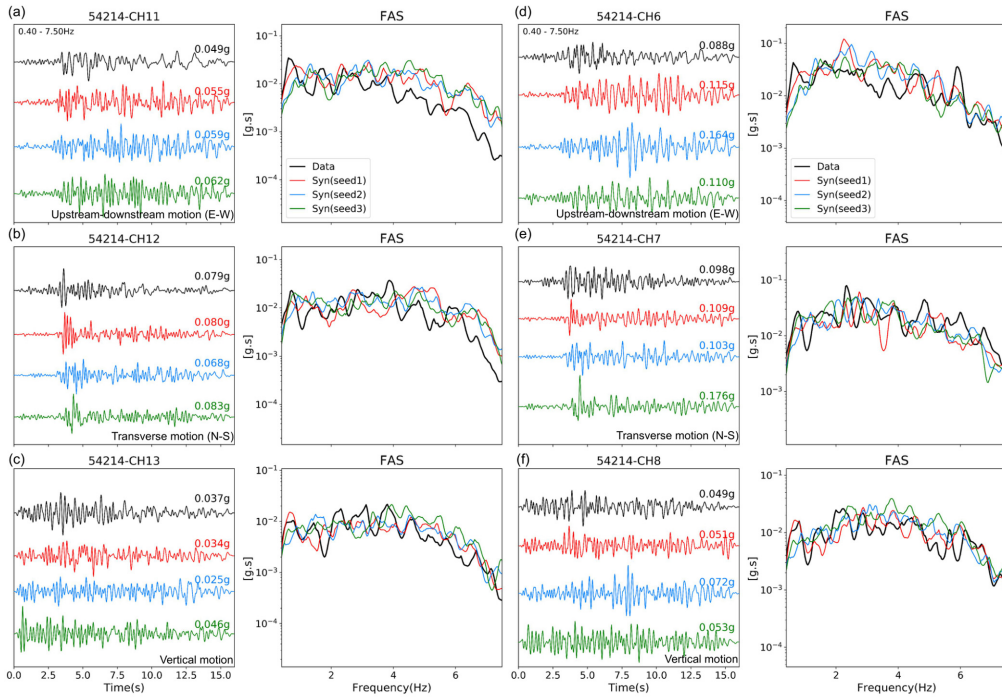


Figure 6. Comparison of data (black traces) and synthetics computed for three realizations of source ruptures (red, blue, and green traces for seeds 1, 2, and 3, respectively) for the 1986 Chalfant Valley earthquake in the time and FAS domains at sensors located near the downstream base (a) to (c) and at the crest center (d) to (f). See Figure 2 for sensor locations. The synthetic traces were computed with CVM-S, a GTL tapered to 700 m below the free surface, and a dam core with $V_S = 450$ m/s, using the source model shown in Supplemental Material Figure S10.

HCF scenarios

As shown above, our validations for the M_w 3.7 and the M_w 6.2 1986 Chalfant Valley earthquakes result in well-calibrated velocity and attenuation models for the LVD and surrounding area. In addition, the results of the modeling of the Chalfant Valley event demonstrate that the Graves and Pitarka (2016) kinematic rupture generator is able to create source descriptions that produce ground motions in agreement with data for frequencies of up to 7.5 Hz. We are therefore ready to perform simulations for scenario earthquakes to estimate ground motions on the LVD for MCE events on the HCF.

Source description

The M_w 6.6 scenario is one of three cases presented in Chen et al. (2014) for assessing the seismic hazard of the Long Valley Caldera area associated with the HCF. In addition to the M_w 6.6 scenario, the study also considered M_w 6.5 and M_w 6.8 scenarios. However, Chen et al. (2014) pointed out that the fault rupture for the M_w 6.8 scenario needs to extend into the Long Valley Caldera with a geometry that violates both geologic and kinematic constraints (Hill and Montgomery-Brown, 2015). Assuming that the expected hazards to the LVD from M_w 6.5 events are smaller, we chose the M_w 6.6 scenario to

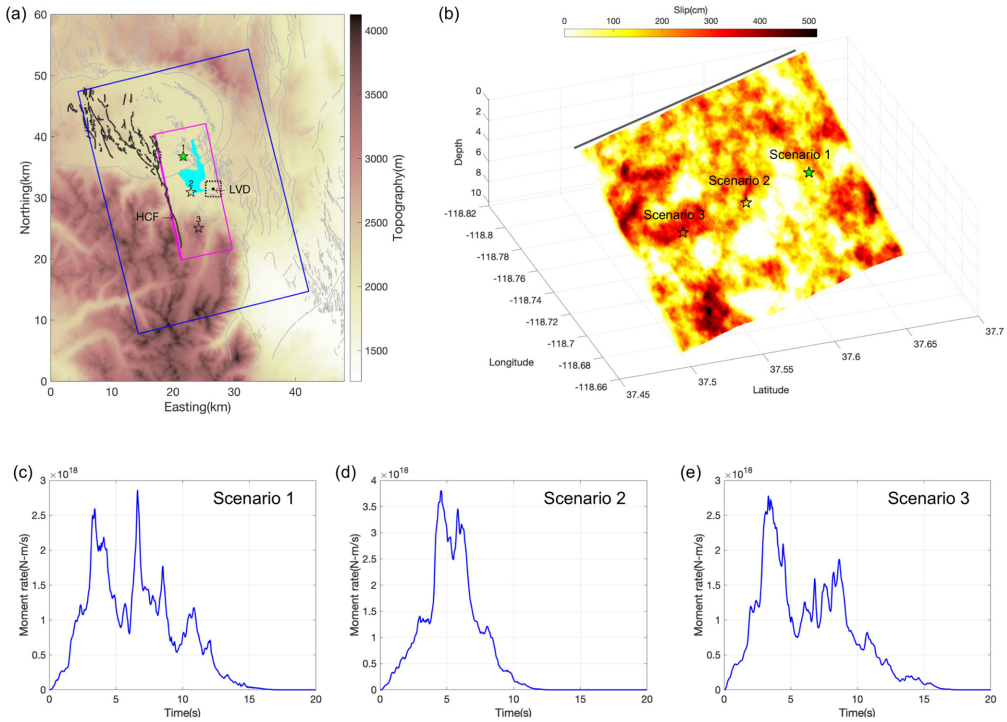


Figure 7. (a) Domains used for the HCF linear elastic simulations (large blue box) and plane wave calculations (dashed box) with the fault plane indicated by the magenta box where the thicker side is the top of the fault. (b) Slip distribution generated for the HCF simulations with stars depicting the three proposed hypocenter locations. The green filled star (scenario 1) in (a) and (b) depicts the hypocentral location of the HCF scenario with southward rupture propagation, which was used for the nonlinear MCE simulations. Moment-rate functions of the three scenarios are shown in (c) to (e).

represent the MCE. Based on the estimate of Chen et al. (2014), the recurrence interval for this scenario is 204 years.

We used the fault orientation from the USGS Quaternary fault and fold database (Haller et al., 2004) for strike and dip of the HCF sources and assumed pure normal faulting. We designed scenarios on the HCF with a fault length of 21 km and a width of 13.3 km, estimated using the empirical magnitude-area relations by Leonard (2010) (see proposed fault plane in Figure 7). Three different rupture scenarios with the same slip distribution were selected to capture the range of ground motions expected from the HCF MCE, with southward, northward, and bilateral rupture propagation (Figure 7). The hypocenters of all three rupture scenarios are located 6 km down-dip from the top of the fault, all featuring surface ruptures. The hypocenter locations of the scenarios with northward and southward rupture propagation are 6 km away from the center of the fault (Figure 7). Source parameters for the HCF scenarios are listed in Table 5.

Elastic and nonlinear properties of materials

For the HCF simulations we used the SCEC CVM-S with the GTL thickness (700 m) and attenuation model ($\gamma = 0$, $Q_S = 0.075V_S$, where V_S is in m/s, and $Q_P = 2Q_S$), constrained by both the M_w 3.7 and Chalfant Valley earthquake validations.

Table 5. Source parameters for the HCF M_w 6.6 MCE scenariosHypocenter location (*Lon.*, *Lat.*, depth)

Scenario with southward rupture:

– 118.7633°, 37.6352°, 4.6 km

Scenario with bilateral rupture:

– 118.7479°, 37.5826°, 4.6 km

Scenario with northward rupture:

– 118.7325°, 37.5299°, 4.6 km

Focal mechanism^a (strike/dip/rake)

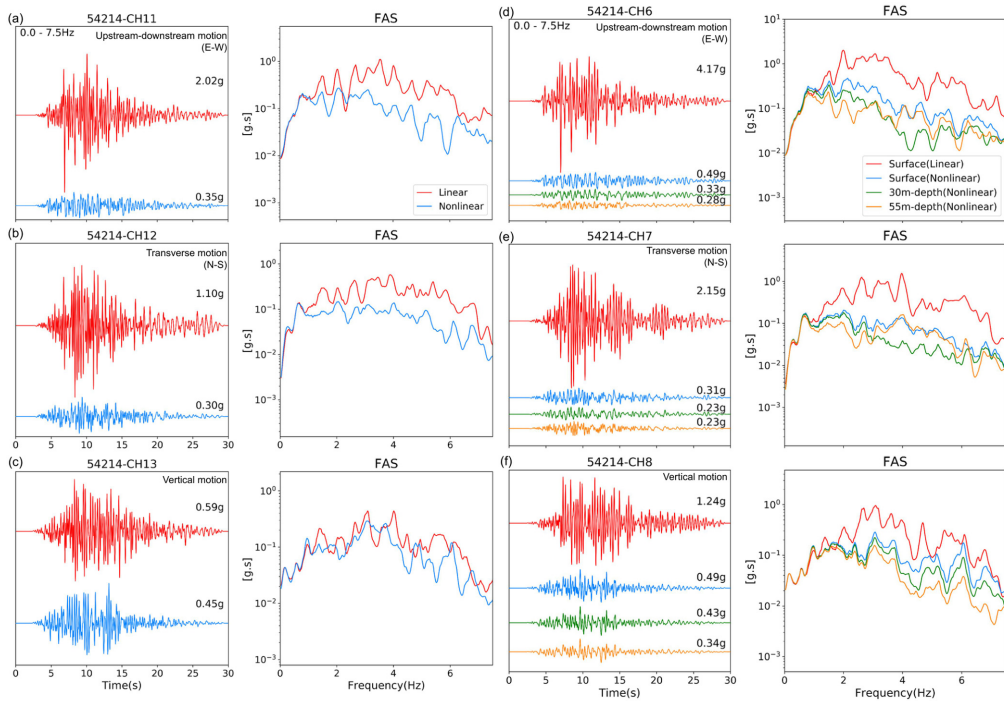
348°/50°/–90°

Fault dimensions^b

Length = 21 km

Width = 13.3 km

HCF: Hilton Creek Fault; MCE: Maximum Credible Earthquake.

^aUS Geological Survey Quaternary fault and fold database (Haller et al., 2004).^bLeonard (2010).**Figure 8.** Comparison of linear (red traces) and nonlinear (blue traces) synthetics computed for the HCF scenario with southward rupture propagation in the time and FAS domains at sensors located near the downstream base (a) to (c) and various depths beneath the crest center (d) to (f), where results for 30 and 50 m beneath the dam crest are shown in green and orange, respectively. See Figure 2 for sensor locations.

As Equation 3 shows, the shear strength of a material depends on the initial stress state and the pore fluid pressure. To account for the shear stress components that balance the horizontal loading due to the 3D structural heterogeneities and the surface topography, we followed the stress relaxation process outlined by Duan and Day (2010). Here, the stress field was first relaxed by applying the gravitational force, without considering nonlinearity. For the relaxation stage, we imposed a fixed condition for both horizontal and vertical

motions along the bottom boundary, along with zero vertical traction and zero horizontal velocity conditions on the (vertical) side boundaries (Duan and Day, 2010). The relaxation stage ends when the largest particle motion in the domain is smaller than a 100th of the peak value. The stress field at the end of the relaxation is considered static equilibrium, and we use it as the initial stress field for the nonlinear calculation.

We consider hydrostatic conditions (Bethke, 1986) for the fluid pressure in Equation 3, calculated by $P = \rho g D$, where ρ is the density of water (1050 kg/m^3), g is the gravitational acceleration (9.81 m/s^2), and D is the depth below the ground water level. The water level inside the dam follows the predefined phreatic line shown in Figure 9. Pore pressure is set to zero for all material above the phreatic line inside the dam. As can be seen in Equation 3, the fluid pressure and the effective mean stress are competing mechanisms at shallow depths where lithostatic loading is relatively weak, implying that including the fluid pressure is crucial when estimating the strength of material near the surface.

The reference strain can be computed from the yield stress using Equation 2. To estimate the yield stress of the material within the dam, we assumed a cohesion of 45 kPa and a friction angle $\phi = 39^\circ$ for the LVD, as was used for the LVD dam core material in Griffiths and Prevost (1988). To determine the strength of the material off the dam, we adopted the generalized Hoek–Brown failure criterion that conveniently provides the effective cohesion and a friction angle needed to compute the yield stress. The Hoek–Brown failure criterion uses a Geological Strength Index (GSI) value for each material. As the mechanical properties of near-surface material are poorly constrained, we make the assumption that GSI is correlated with the local shear wave speed (V_S). The V_S and GSI measurements for rock samples in southern California by Townsend et al. (2021) (Figure 5 of their study) illustrate the relationship between these two quantities. Their analysis shows that (1) rocks with V_S of 200–300 m/s can be characterized by a GSI of 20, (2) GSI of rock samples with V_S of 300–500 m/s fall in the 20–40 range, and (3) rocks with V_S of 1500 m/s are usually associated with GSI values of ~ 90 . Based on these observations, we first assigned each material into a category based on its S-wave speed, and used the corresponding relationship to compute the GSI value:

$$GSI = \begin{cases} 20 & \text{if } V_S < 300 \text{ m/s} \\ 20 + (V_S - 300) \times \frac{40 - 20}{500 - 300} & \text{if } 300 \text{ m/s} \leq V_S < 500 \text{ m/s} \\ 40 + (V_S - 500) \times \frac{90 - 40}{1500 - 500} & \text{if } 500 \text{ m/s} \leq V_S < 1500 \text{ m/s} \\ 90 + (V_S - 1500) \times \frac{100 - 90}{2000 - 1500} & \text{if } 1500 \text{ m/s} \leq V_S < 2000 \text{ m/s} \\ 100 & \text{if } V_S \geq 2000 \text{ m/s} \end{cases}$$

Following the above approach to compute reference strains, Supplemental Material Figure S14 demonstrates the vertical profiles of nonlinear parameters beneath the crest center of the LVD.

HCF scenario ground motion results

As a reference, and to estimate the source parameters of a “worst case” scenario we first performed linear simulations for the proposed HCF scenarios. Here, we examined three slip realizations for each of three hypocentral locations. As was the case for the Chalfant

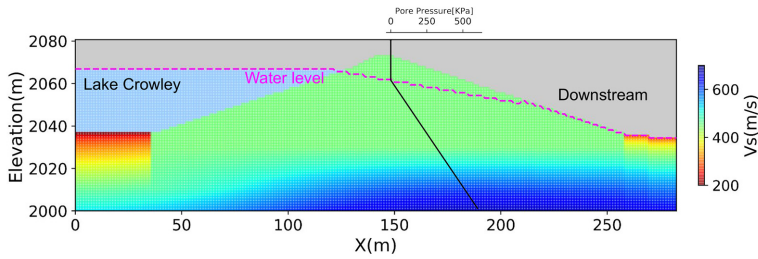


Figure 9. Cross section of V_s through the LVD along the white line in Figure 2. The dashed line depicts the water level assumed for the nonlinear simulations, and the pore pressure as a function of depth is shown by the solid line.

Valley validation event, the PGAs at the LVD do not significantly vary with the random seed number for the same HCF rupture scenarios. Among the three hypocentral locations, the scenario with southward rupture propagation generated the largest PGAs at the center of the dam crest, which was therefore selected for our nonlinear simulations. See Supplemental Material Figures S15 to S17, for comparisons of synthetic waveforms and spectra.

We performed 3D linear simulations in the entire model domain (see blue box in Figure 7a, and simulation parameters in Table 6). However, high computational cost limited our simulations with Iwan nonlinearity using 10 yield surfaces to a 2.5 by 2.5 km area that includes only the LVD and the immediate surrounding areas (dashed box in Figure 7a). To reduce the computational cost we applied a two-step method, similar in scope to the Domain Reduction Domain finite-element approach proposed by Bielak et al. (2003). We used the three-component velocity waveforms calculated at a depth of 1260 m below the crest of the dam from the full-domain 3D linear simulation for the scenario with southward rupture propagation as a vertically incident, up-going plane wave source, inserted at the same depth below the dam in the small domain. The source-insertion depth of 1260 m was selected as an optimal choice, sufficiently deep to exclude near-source nonlinearity and to include all significant nonlinear effects and structural coupling in the small domain, and sufficiently shallow to avoid unnecessary computational cost.

Using this two-step approach, we were able to achieve an adequate representation of hysteretic behavior using 10 yield surfaces while the coupling between the LVD and the surrounding 3D structures can still be fully accounted for in our calculations. Table 7 provides technical details about this calculation domain. We verified the accuracy of this approach by comparing the linear synthetic waveforms computed using the two-step method against those computed in a single step in the full domain (see Supplemental Material, Figures S18 to S21), with spectral bias on average of 26% over all the sensor locations shown in Figure 2, with the largest bias around 1 Hz. The two-step approach is therefore deemed a fair approximation to the full-domain 3D simulation and was used in the following calculations. Furthermore, the use of the smaller domain for the dam in the two-step method allowed a reduced grid spacing of 1.25 m, which is necessary to maintain numerical accuracy considering the reduction of shear moduli from the strong nonlinear effects. The smaller grid spacing enabled a more detailed description of the dam surface, further reducing the inaccuracies from the use of the vacuum formulation.

Figure 8 shows acceleration waveforms and FAS for linear and nonlinear simulations at the downstream base ((a) to (c)) and the surface of the crest center as well as at 30 and

Table 6. Simulation parameters of the full-domain linear simulations for the HCF M_w 6.6 MCE scenarios

Domain	
Length	28.72 km
Width	40.82 km
Depth	30.68 km
Southwest corner	-118.8402°, 37.3725°
Northwest corner	-118.9611°, 37.7275°
Southeast corner	-118.5268°, 37.4397°
Northeast corner	-118.6463°, 37.7950°
Rotation angle	14.01° counterclockwise from north
Geodetic datum	WGS84
UTM zone	11
Spatial resolution	
Maximum frequency	7.5 Hz
Minimum V_s	175 m/s
Points per minimum wavelength	6.7
Grid spacing	3.5 m: 4.23 km above sea level to 0.24 km below sea level 10.5 m: 0.22–2.56 km below sea level 31.5 m: 2.49–30.68 km below sea level
Temporal resolution	
Time step	0.00027 s
Simulation time	30 s

HCF: Hilton Creek Fault; MCE: maximum credible earthquake; UTM: Universal Transverse Mercator.

Table 7. Simulation parameters of the smaller domain used in the two-step calculations for the nonlinear HCF M_w 6.6 MCE scenarios

Domain	
Length	2.52 km
Width	2.52 km
Depth	2.56 km
Southwest corner	-118.7204°, 37.5765°
Northwest corner	-118.7209°, 37.5992°
Southeast corner	-118.6919°, 37.5769°
Northeast corner	-118.6924°, 37.5996°
Rotation angle	0°
Geodetic datum	WGS84
UTM zone	11
Spatial resolution	
Maximum frequency	7.5 Hz
Minimum V_s	175 m/s
Points per minimum wavelength	18.7
Grid spacing	1.25 m
Temporal resolution	
Time step	0.00013 s
Simulation time	30 s

HCF: Hilton Creek Fault; MCE: maximum credible earthquake; UTM: Universal Transverse Mercator.

55 m depth ((d) to (f)). A comparison of the linear ground motions shows that the dam structure amplifies the ground motions by about a factor of 2. The reduction of the PGAs due to nonlinear response of the material is large, up to a factor of about 8, with larger reductions on the crest as compared with off the dam (e.g. CH6, 7, and 8 in Figure 8d to f vs a factor of 7 at CH11, 12, and 13 in Figure 8a to c). Additional waveform comparisons

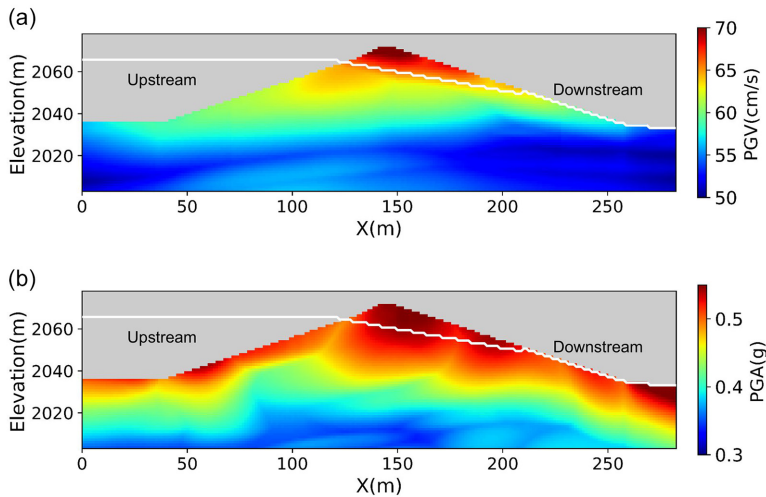


Figure 10. (a) PGV and (b) PGA from HCF scenario 1 in Figure 7 along the transect shown by the white line in Figure 2. The white line depicts the phreatic line.

at other locations on the dam can be found in Figures S22 to S24 in the Supplemental Material. These results indicate that nonlinear effects are significantly affecting the ground motions inside the LVD. Moreover, it is clear that the high-frequency signal present in the acceleration waveforms at the bottom of the dam vanishes toward the crest top due to nonlinear damping. For example, the FAS results for the horizontal components show that the elevated energy between 4 and 6 Hz in the waveforms 55 m below the dam crest is reduced in the record 30 m below the dam crest, where the energy between 2 and 4 Hz is enhanced.

On the contrary, the vertical ground motions show monotonic increase of amplitudes approaching the crest top without the high-frequency energy depletion found on the horizontal components (Supplemental Material Figure S28 and Figure 8f). The reason for this is likely that the vertical component primarily contains P-waves which are inefficient in triggering nonlinearity. Figures S26 to S28 in the Supplemental Material show synthetic time histories at a higher density inside the dam.

We use transects across the dam (Figure 9, along the white line in Figure 2) to further demonstrate the nonlinear ground motion response of the dam for the HCF scenario. Figure 10 shows that both peak ground velocities (PGVs) and PGAs are amplified along the surface of the dam. The largest PGVs ($\sim 72\text{m/s}$) and PGAs ($\sim 0.55\text{ g}$) occur near the crest top, in particular in the region between the downstream face and the phreatic line. This is expected as the material above the phreatic line is exposed to less nonlinear damping due to lack of fluid pressure, and therefore stronger ground motions due to higher yield stresses.

Settlement of the dam after a seismic event is important information for evaluating stability of the dam, which here is obtained from the displacement field at the end of the simulation. Figure 11 depicts the total displacement on all three components inside the dam along the transect. Our nonlinear simulation predicts larger eastward displacements (up to $\sim 45\text{ cm}$) near the lower part of the downstream face, as compared with those on

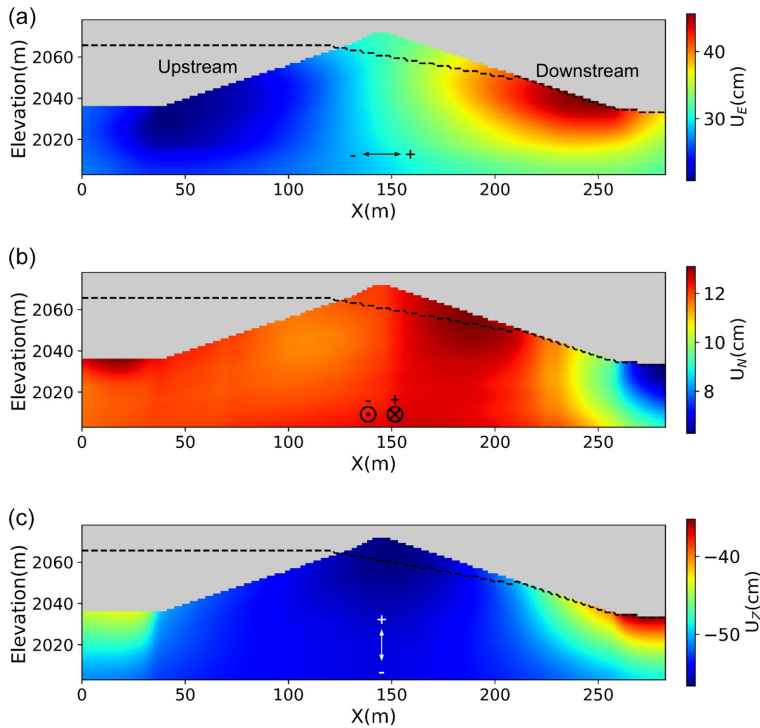


Figure 11. Predicted displacement field inside the LVD from HCF scenario I in Figure 7. The dashed line depicts the phreatic line. (a) Upstream–downstream displacement. (b) Transverse displacement. (c) Vertical displacement.

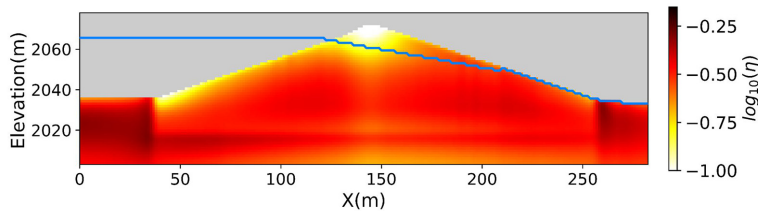


Figure 12. Accumulated material damage (η) in LVD from HCF scenario I in Figure 7.

the upstream side (~ 18 cm), suggesting a relative movement of up to ~ 27 cm inside the dam toward the downstream side. Vertically, the simulation predicts generally downward movement at the dam due to the normal faulting mechanism of the HCF scenario. Our nonlinear model predicts subsidence of ~ 55 cm for the material at the crest of the LVD, along with ~ 35 and ~ 45 cm near the downstream and the upstream base, respectively.

In addition to settlement of the LVD, we calculated the accumulated strain values, η (Figure 12). As mentioned in Ma and Andrews (2010), this quantity is a good representation of actual material damage, since it is the cumulative norm of the strain-tensor increments throughout the simulation and thus does not decay through time. The largest accumulated strain (30%–35%) occurs in the middle of the dam, ~ 20 m below the surface

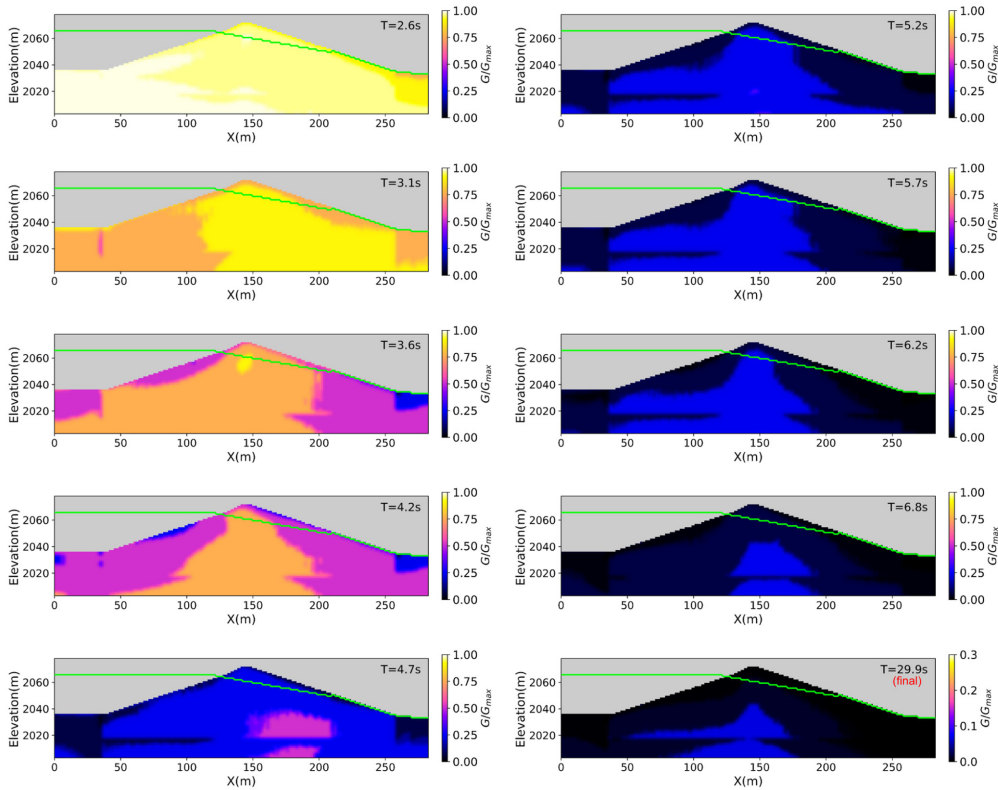


Figure 13. Snapshots of lowest encountered $\frac{G}{G_{\max}}$ values as of the indicated time within the cross section depicted in Figure 9. Note the different color scale for the final panel.

of both upstream and downstream faces. Our simulation predicts more damage on the downstream side than the upstream side. The simulation predicts relatively lower permanent strain near the crest ($\sim 8\%$).

Finally, our nonlinear approach allows us to depict the reduction of the shear modulus due to nonlinear damping as the wavefield impinges onto the dam. Figure 13 shows the lowest encountered value of the shear modulus G as of the indicated time on each snapshot, normalized by the low-strain shear modulus G_{\max} , for a range of times during the nonlinear simulation. Note that the G/G_{\max} values can only assume as many different values as the number of yield surfaces (here, 10). The largest reductions generally start from the free surface caused by lower yield stress. The largest reduction in the shear modulus (about 90%) inside the dam occurs right below the surface on both the upstream and downstream sides, as waves with the largest amplitudes arrive at the LVD around 5–6 s. Note that the final snapshot captures the lowest values throughout the entire simulation time.

Discussion and future work

The goal of this study is to predict broadband ground motions for MCE scenarios at the LVD. To ensure that our predicted ground motions are accurate, we first conducted two validations, namely, using (1) a M_w 3.7 event in 2015 with a point source representation and (2) the M_w 6.2 Chalfant Valley earthquake of 1986 modeled by finite-fault sources in

the linear regime. During the first validation, we calibrated the tapering depth for the near-surface GTL representation to $z_T = 700\text{m}$. Furthermore, we estimated the optimal anelastic attenuation as $Q_s(f) = 0.075V_S$ (V_S in m/s) without dependence on frequency ($\gamma = 0$), for the dam and the surrounding areas. Using this calibrated model, we showed that our numerical simulation results can generate 0–7.5 Hz wavefields that are in good agreement with data. The simulations of the MCE scenarios for the HCF were carried out adopting the calibrated model parameters.

Although the seismic response of the LVD has been extensively studied, there is to our knowledge no direct measurements of the material properties of the LVD available. A numerical study of the seismic response of the LVD by Yiagos and Prevost (1991) used an exponential function to assign V_S increasing with depth. On the contrary, Griffiths and Prevost (1988) assigned material properties to discrete layers of the dam, including a thin, shallow layer representing the rock shell. Our simulations using the elastic parameters adopted in these studies significantly overpredicted the peak seismic amplitudes on the dam, due to the presence of material with low seismic speed at the shallowest depth. A possible explanation for this discrepancy is that V_S of the rock shell has increased over time due to variation of the water level (Clariá and Rinaldi, 2007; Dong and Lu, 2016) or internal deterioration. However, future work is needed to address this issue, such as through shallow seismic surveys on the dam.

The M6.6 HCF scenarios are similar to the largest event (M_L 6.7) in the 1980 Mammoth Lake earthquake series (Lai and Seed, 1985; Zeghal and Abdel-Ghaffar, 2009) in terms of magnitude, faulting mechanism, and distance to the LVD. It is thus encouraging that the largest PGAs recorded on the LVD during the 1980 M_L 6.7 Mammoth Lake earthquake event (~ 0.55 g) are similar to those obtained in our nonlinear HCF simulations, which lends some credibility to the reference strain values used in our simulations. Furthermore, our estimated PGA values on the LVD crest are similar to those obtained from previous numerical studies of the dam, all of them with a source consisting of a recording of the 1980 M6.7 Mammoth Lake, CA, earthquake, located just off the dam (downstream toe channels). Griffiths and Prevost (1988) used a multi-surface plasticity model, Yiagos and Prevost (1991) a two-phase elasto-plastic method, and Ebrahimian (2011) an elastic-perfectly plastic approach including extended Masing rules. The estimated PGA on the LVD crest from our study (0.55 g) compares well with the values of 0.47 g estimated by Griffiths and Prevost (1988), 0.65 g by Yiagos and Prevost (1991), and 0.6 g by Ebrahimian (2011), considering the differences in the modeling methods. In addition, we find that PGA values are reduced from the crest center to the north and south ends of the crest (see Supplemental Material Figures S22 and S23, channels 4–5 and 14–16) by up to about 22%, a similar spatial variation as predicted by Griffiths and Prevost (1988) for the 1980 M_L 6.7 Mammoth earthquake.

As mentioned in section “Near-surface GTL and $Q(f)$,” our model, unlike conventional studies, includes a GTL below the dam (with a minimum V_S of 540 m/s), in addition to the surroundings of the structure. We find that the peak acceleration of our input plane wave source (0.49 g) is reduced by about 43% from the source depth by the time it arrives at the base of the dam (0.28 g) on the horizontal components, which are primarily affected by nonlinearity. This is significant, as we would have overpredicted the PGA at the dam crest by a factor of 1.75 if the GTL had been omitted. It is interesting to note that other numerical nonlinear studies of the LVD that omitted the GTL (e.g. Ebrahimian, 2011; Griffiths and Prevost, 1988) estimated PGA values on the dam in agreement with data for the 1980 M6.7 Mammoth Lake event (about 0.5 g). The reason for this is likely that they used a

source consisting of the data recorded off the dam, which already included the (linear and nonlinear) effects of the GTL.

The uncertainty of the estimated HCF MCE ground motions depends on that of several factors in the modeling. In addition to the uncertainty of the elastic parameters of the dam mentioned above, the ground motions are expected to vary significantly with the nonlinear properties of the material of the dam and surrounding low-velocity material, as shown by Roten et al. (2014, 2018). To estimate a realistic range of the resulting peak ground motions considering the uncertainties in the nonlinear properties of the dam and the underlying material, we followed the approach by Roten et al. (2023) and performed additional nonlinear simulations with lower and upper bounds on the reference strain. Darendeli (2001) provided an expression for the standard deviation of the normalized shear modulus reduction curve, which has a simplified form for $\frac{G}{G_{max}} = 0.5$ as:

$$\sigma = \exp(\phi_{13}) + \sqrt{\frac{0.25}{\exp(\phi_{14})}} = 0.09638, \quad (10)$$

where $\phi_{13} = -4.23$, $\phi_{14} = 3.62$ from their Table 8.12. By adding and subtracting one standard deviation in Equation 10 to the $\frac{G}{G_{max}}$ curve and determining the strain value corresponding to $\frac{G}{G_{max}} = 0.5$ (i.e. the reference strain), we derived the lower and upper bounds of the reference strain model shown in Supplemental Material Figure S29. We find 26%–48% variations in the PGA values for the horizontal motions relative to the predicted values for the proposed nonlinear model shown in Figure 8, and 6%–12% variations on the vertical component (see Supplemental Material Figure S30 for waveform comparisons). We note that this range of ground motions does not include uncertainties in the elastic properties of the shallow structure. Future studies should focus on acquiring more robust constraints on both the elastic and nonlinear properties of the LVD and the surrounding shallow crust. Finally, we recommend that ground motions be estimated for a large ensemble of source descriptions, to capture a realistic range of slip distributions, rupture times, and hypocentral locations.

The computational requirements for the simulations in this study are significant, in particular for those in the nonlinear regime. As noted by Roten et al. (2023), each of the nonlinear simulations in our study requires at least 5 times the GPU memory space compared with a linear run of the same size using 10 yield surfaces, while the calculation time per time step also increases. Additional GPUs might be required on supercomputers with limitations on wall clock time to shorten the time for the entire calculation to complete. As a result, the actual computational cost of a nonlinear run in this study is approximately 60 times that of a linear simulation.

The results of this study can be used as a direct input for further evaluation of the structural stability of the LVD considering the MCE scenarios. While beyond our expertise and scope of this study, we recommend such assessment as important future work.

Acknowledgments

The authors are grateful for the critical reviews and constructive comments by Jeff Bayless, Brad Aagaard, and an anonymous reviewer who contributed to an improved article.


Declaration of conflicting interests

The author(s) declared no potential conflicts of interest with respect to the research, authorship, and/or publication of this article.

Funding

The authors disclosed receipt of the following financial support for the research, authorship, and/or publication of this article: This research was supported through the California Geological Survey (Award #1020-006), the National Science Foundation under Grant No. EAR-1664203, and the Statewide California Earthquake Center (SCEC; Contribution No. 13351). SCEC is funded by National Science Foundation (NSF) Cooperative Agreement EAR-1600087 and US Geological Survey (USGS) Cooperative Agreement G17AC00047.

ORCID iD

Te-Yang Yeh  <https://orcid.org/0000-0002-9146-6804>

Data and resources

This research used resources of the Oak Ridge Leadership Computing Facility at the Oak Ridge National Laboratory, which is supported by the Office of Science of the US Department of Energy under Contract No. DE-AC05-00OR22725. Corrected strong-motion seismic data can be accessed from the website of CESMD Strong Motion Data Set (<https://www.strongmotioncenter.org>).

Supplemental material

Supplemental material for this article is available online.

References

- Bethke CM (1986) Inverse hydrologic analysis of the distribution and origin of Gulf Coast-type geopressured zones. *Journal of Geophysical Research: Solid Earth* 91: 6535–6545.
- Bielak J, Loukakis K, Hisada Y and Yoshimura C (2003) Domain reduction method for three-dimensional earthquake modeling in localized regions. *Bulletin of the Seismological Society of America* 93: 817–824.
- Brune JN (1970) Tectonic stress and the spectra of seismic shear waves from earthquakes. *Journal of Geophysical Research* 75: 4997–5009.
- California Geological Survey (1972) California strong motion instrumentation program. DOI: 10.7914/B34Q-BB70.
- Cascone E, Biondi G, Aliberti D and Rampello S (2021) Effect of vertical input motion and excess pore pressures on the seismic performance of a zoned dam. *Soil Dynamics and Earthquake Engineering* 142: 106566.
- Chen R, Branum DM, Wills CJ and Hill DP (2014) Scenario earthquake hazards for the Long Valley Caldera-Mono Lake area, east-central California (Version 2.0, January 2018). Open-file report. US Geological Survey. DOI: 10.3133/ofr20141045.
- Clariá JJ and Rinaldi VA (2007) Shear wave velocity of a compacted clayey silt. *Geotechnical Testing Journal* 30: 399–408.
- Cockerham RS and Corbett EJ (1987) The July 1986 Chalfant Valley, California, earthquake sequence: Preliminary results. *Bulletin of the Seismological Society of America* 77: 280–289.
- Cui EY, Poyraz Olsen KB, Zhou J, Withers K, Callaghan S, Larkin J, Guest C, Choi D, Chourasia A, Shi Z, Day S, Maechling J and Jordan TH (2013) Physics-based seismic hazard analysis on petascale heterogeneous supercomputers. DOI: 10.1109/SC.2010.45.

- Darendeli MB (2001) *Development of a New Family of Normalized Modulus Reduction and Material Damping Curves*. Austin, TX: The University of Texas at Austin.
- Dong Y and Lu N (2016) Dependencies of shear wave velocity and shear modulus of soil on saturation. *Journal of Engineering Mechanics* 142: 04016083.
- Duan B and Day SM (2010) Sensitivity study of physical limits on ground motion at Yucca Mountain. *Bulletin of the Seismological Society of America* 100: 2996–3019.
- Dziewonski AM, Chou T-A and Woodhouse JH (1981) Determination of earthquake source parameters from waveform data for studies of global and regional seismicity. *Journal of Geophysical Research: Solid Earth* 86: 2825–2852.
- Ebrahimian B (2011) Numerical analysis of nonlinear dynamic behavior of earth dams. *Frontiers of Architecture and Civil Engineering in China* 5: 24–40.
- Ekström G, Nettles M and Dziewoński AM (2012) The global CMT project 2004–2010: Centroid-moment tensors for 13,017 earthquakes. *Physics of the Earth and Planetary Interiors* 200–201: 1–9.
- Elia G and Rouainia M (2013) Seismic performance of earth embankment using simple and advanced numerical approaches. *Journal of Geotechnical and Geoenvironmental Engineering* 139: 1115–1129.
- Ely GP, Jordan T, Small P and Maechling PJ (2010) *A VS30-Derived Near-Surface Seismic Velocity Model*. San Francisco, CA: American Geophysical Union.
- Eshelby JD (1957) The determination of the elastic field of an ellipsoidal inclusion, and related problems. *Proceedings of the Royal Society of London. Series A: Mathematical and Physical Sciences* 241: 376–396.
- FEMA (2005) Federal guidelines for dam safety: Earthquake analyses and design of dams. FEMA 65. https://www.fema.gov/sites/default/files/2020-08/fema_dam-safety_earthquake-analysis_P-65.pdf
- Graves RW (1996) Simulating seismic wave propagation in 3D elastic media using staggered-grid finite differences. *Bulletin of the Seismological Society of America* 86: 1091–1106.
- Graves RW and Pitarka A (2016) Kinematic ground-motion simulations on rough faults including effects of 3D stochastic velocity perturbations. *Bulletin of the Seismological Society of America* 106: 2136–2153.
- Griffiths DV and Prevost JH (1988) Two- and three-dimensional dynamic finite element analyses of the Long Valley Dam. *Géotechnique* 38: 367–388.
- Haller KM, Machette MN, Dart RL and Rhea BS (2004) US quaternary fault and fold database released. <https://doi.org/10.5066/P9BCVRCK>
- Hardin BO and Drnevich VP (1972) Shear modulus and damping in soils: Design equations and curves. *Journal of the Soil Mechanics and Foundations Division* 98: 667–692.
- Hill DP and Montgomery-Brown E (2015) Long Valley Caldera and the UCERF depiction of Sierra Nevada range-front faults. *Bulletin of the Seismological Society of America* 105: 3189–3195.
- Hu Z, Olsen KB and Day SM (2022a) 0–5 Hz deterministic 3-D ground motion simulations for the 2014 La Habra, California, earthquake. *Geophysical Journal International* 230: 2162–2182.
- Hu Z, Olsen KB and Day SM (2022b) Calibration of the near-surface seismic structure in the SCEC community velocity model version 4. *Geophysical Journal International* 230: 2183–2198.
- Iwan WD (1967) On a class of models for the yielding behavior of continuous and composite systems. *Journal of Applied Mechanics* 34: 612–617.
- Kaklamanos J, Dorfmann L and Baise LG (2015) A simple approach to site-response modeling: The overlay concept. *Seismological Research Letters* 86: 413–423.
- Kanamori H and Anderson DL (1975) Theoretical basis of some empirical relations in seismology. *Bulletin of the Seismological Society of America* 65: 1073–1095.
- Lai S and Seed HB (1985) *Dynamic Response of Long Valley Dam in the Mammoth Lake Earthquake Series of May 25–27, 1980 (142304)*. Berkeley, CA: College of Engineering, University of California.
- Leonard M (2010) Earthquake fault scaling: Self-consistent relating of rupture length, width, average displacement, and moment release. *Bulletin of the Seismological Society of America* 100: 1971–1988.

- Ma S and Andrews DJ (2010) Inelastic off-fault response and three-dimensional dynamics of earthquake rupture on a strike-slip fault. *Journal of Geophysical Research: Solid Earth* 115.
- Madariaga R (1976) Dynamics of an expanding circular fault. *Bulletin of the Seismological Society of America* 66: 639–666.
- Maechling PJ, Silva F, Callaghan S and Jordan TH (2014) SCEC broadband platform: System architecture and software implementation. *Seismological Research Letters* 86: 27–38.
- Masing G (1926) Eigenspannumyen und verfeshung beim messing. In: *Proceedings of the international congress for applied mechanics*, Zurich, Switzerland, pp. 332–335.
- Mróz Z (1967) On the description of anisotropic workhardening. *Journal of the Mechanics and Physics of Solids* 15: 163–175.
- Nie S, Wang Y, Olsen KB and Day SM (2017) Fourth-order staggered-grid finite-difference seismic wavefield estimation using a discontinuous mesh interface (WEDMI) fourth-order staggered-grid finite-difference seismic WEDMI. *Bulletin of the Seismological Society of America* 107: 2183–2193.
- Okamoto T and Takenaka H (2005) Fluid-solid boundary implementation in the velocity-stress finite-difference method. *Journal of the Seismological Society of Japan* 57: 355–364.
- Olsen KB (1994) *Simulation of three-dimensional wave propagation in the Salt Lake Basin*. PhD Thesis, The University of Utah, Salt Lake City, UT.
- Olsen KB, Day SM and Bradley CR (2003) Estimation of Q for long-period (>2 sec) waves in the Los Angeles Basin. *Bulletin of the Seismological Society of America* 93: 627–638.
- O'Reilly O, Yeh T, Olsen KB, Hu Z, Breuer A, Roten D and Goulet CA (2022) A high-order finite-difference method on staggered curvilinear grids for seismic wave propagation applications with topography. *Bulletin of the Seismological Society of America* 112: 3–22.
- Pacheco J and Nábělek J (1988) Source mechanisms of three moderate California earthquakes of July 1986. *Bulletin of the Seismological Society of America* 78: 1907–1929.
- Pelecanos L, Kontoe S and Zdravkovic L (2012) Numerical analysis of the seismic response of La Villita Dam in Mexico. In: *17th BDS (British dam society) conference*, Leeds, UK, September.
- Prejean SG and Ellsworth WL (2001) Observations of earthquake source parameters at 2 km depth in the Long Valley Caldera, Eastern California. *Bulletin of the Seismological Society of America* 91: 165–177.
- Randall CJ (1989) Absorbing boundary condition for the elastic wave equation: Velocity-stress formulation. *Geophysics* 54: 1141–1152.
- Roten D, Olsen KB and Pechmann JC (2012) 3D simulations of M 7 earthquakes on the Wasatch fault, Utah, part II: Broadband (0–10 Hz) ground motions and nonlinear soil behavior. *Bulletin of the Seismological Society of America* 102: 2008–2030.
- Roten D, Olsen KB, Day SM and Cui Y (2018) Quantification of fault-zone plasticity effects with spontaneous rupture simulations. In: Dalguer LA, Fukushima Y, Irikura K and Wu C (eds) *Best Practices in Physics-based Fault Rupture Models for Seismic Hazard Assessment of Nuclear Installations*. Cham: Springer International Publishing, pp. 45–67.
- Roten D, Olsen KB, Day SM, Cui Y and Fäh D (2014) Expected seismic shaking in Los Angeles, reduced by San Andreas fault zone plasticity. *Geophysical Research Letters* 41: 2769–2777.
- Roten D, Yeh T-Y, Olsen K, Day S and Cui Y (2023) Implementation of Iwan-type nonlinear rheology in a 3D high-order staggered-grid finite-difference method. *Bulletin of the Seismological Society of America* 113: 2275–2291.
- Savage JC and Gross WK (1995) Revised dislocation model of the 1986 Chalfant Valley earthquake, eastern California. *Bulletin of the Seismological Society of America* 85: 629–631.
- Savitzky A and Golay MJ (1964) Smoothing and differentiation of data by simplified least squares procedures. *Analytical Chemistry* 36: 1627–1639.
- Seed HB, Makdisi FI and Alba PD (1978) Performance of earth dams during earthquakes. *Journal of the Geotechnical Engineering Division* 104: 967–994.
- Small P, Gill D, Maechling PJ, Taborda R, Callaghan S, Jordan TH, Olsen KB, Ely GP and Goulet C (2017) The SCEC unified community velocity model software framework. *Seismological Research Letters* 88: 1539–1552.

- Smith KD and Priestley KF (2000) Faulting in the 1986 Chalfant, California, sequence: Local tectonics and earthquake source parameters. *Bulletin of the Seismological Society of America* 90: 813–831.
- Thompson EM (2018) An updated Vs30 map for California with geologic and topographic constraints. *US geological survey data release*. DOI: 10.5066/F7JQ108S.
- Townsend KF, Clark MK and Zekkos D (2021) Profiles of near-surface rock mass strength across gradients in Burial, Erosion, and time. *Journal of Geophysical Research: Solid Earth* 126: e2020JF005694.
- US Geological Survey (2020) 3D elevation program 1-meter resolution digital elevation model (Published 20200330). <https://www.usgs.gov/3d-elevation-program>
- US Geological Survey, Earthquake Hazards Program (2017) Advanced National Seismic System (ANSS) comprehensive catalog of earthquake events and products. DOI: 10.5066/F7MS3QZH.
- Wen W, Ji D and Zhai C (2020) Effects of ground motion scaling on the response of structures considering the interdependency between intensity measures and scale factors. *Engineering Structures* 209: 110007.
- Withers KB, Olsen KB and Day SM (2015) Memory-efficient simulation of frequency-dependent QMemory-efficient simulation of frequency-dependent Q. *Bulletin of the Seismological Society of America* 105: 3129–3142.
- Yeh T and Olsen KB (2023) Fault damage zone effects on ground motions during the 2019 Mw 7.1 Ridgecrest, California, earthquake. *Bulletin of the Seismological Society of America* 113: 1724–1738.
- Yiagos AN and Prevost JH (1991) Two-phase elasto-plastic seismic response of earth dams: Applications. *Soil Dynamics and Earthquake Engineering* 10: 371–381.
- Yong A, Thompson EM, Wald DJ, Knudsen KL, Odum JK, Stephenson WJ and Haefner S (2016) *Compilation of VS30 data for the United States*. Report 978. Reston, VA. DOI: 10.3133/ds978.
- Zahradník J, Moczo P and Hron F (1993) Testing four elastic finite-difference schemes for behavior at discontinuities. *Bulletin of the Seismological Society of America* 83: 107–129.
- Zeghal M and Abdel-Ghaffar AM (1992) Analysis of behavior of earth dam using strongmotion earthquake records. *Journal of Geotechnical Engineering* 118: 266–277.
- Zeghal M and Abdel-Ghaffar AM (2009) Evaluation of the nonlinear seismic response of an earth dam: Nonparametric system identification. *Journal of Earthquake Engineering* 13: 384–405.
- Zou D, Xu B, Kong X, Liu H and Zhou Y (2013) Numerical simulation of the seismic response of the Zipingpu concrete face rockfill dam during the Wenchuan earthquake based on a generalized plasticity model. *Computers and Geotechnics* 49: 111–122.